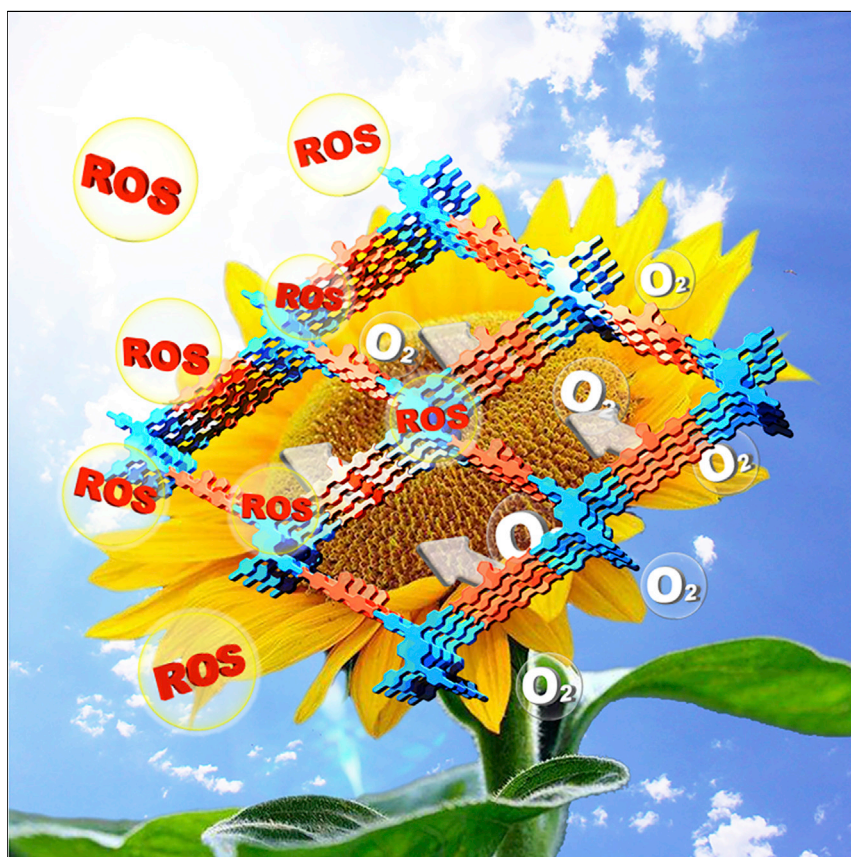**Article**

Programming Covalent Organic Frameworks for Photocatalysis: Investigation of Chemical and Structural Variations

By virtue of the tailorable synthesis of porous organic photosensitizers, we establish the first relationships between their composition, crystallinity, lattice symmetry, and photoreactivity, offering valuable insights for the design of high-performance photocatalysts. In addition to illustrating the dominant paradigm for targeting efficient photocatalysts based on the optical absorption, we experimentally demonstrated that the role of lattice symmetry on the material's photoreactivity indicates that the four-arm core covalent organic frameworks (COFs) are superior to three-arm core COFs in terms of charge-carrier lifetime and, thereby, efficiency.

3 **Understanding**
Dependency and conditional studies
on material behavior

Sai Wang, Qi Sun, Wei Chen, ...,
Lukasz Wojtas, Shengqian Ma,
Feng-Shou Xiao

sunqichs@zju.edu.cn (Q.S.)
sqma@usf.edu (S.M.)
fsxiao@zju.edu.cn (F.-S.X.)

HIGHLIGHTS

The modularity of COFs allows
accelerated photocatalyst design
and discovery

Topology is crucial for a longer
charge-carrier lifetime of COFs

Electronic properties of the paired
struts affect the COFs' optical
properties

Improving the materials'
crystallinity allows for extended
photoadsorption

Article

Programming Covalent Organic Frameworks for Photocatalysis: Investigation of Chemical and Structural Variations

Sai Wang,[1,3] Qi Sun,[2,*] Wei Chen,[4] Yongquan Tang,[1] Briana Aguila,[3] Yanxiong Pan,[5] Anmin Zheng,[4] Zhongyu Yang,[5] Lukasz Wojtas,[3] Shengqian Ma,[3,6,*] and Feng-Shou Xiao[1,*]

SUMMARY

There has been a surge of interest in light-driven chemical transformations using organic photoredox catalysts, whereby a suitable energy alignment and efficient exciton migration are crucial for achieving high efficiency. We show here that covalent organic frameworks (COFs) offer the flexibility required to be ideal platforms for photocatalyst design, lending themselves to fine control over photoreactivity. To understand the factors that dictate photoreactivity, we explore a comparative study of a series of porous materials built with amine bonds with varied composition, crystallinity, and topology, in the efficiency of photogenerated reactive oxygen species. Combined spectroscopies, density functional theory calculations, and catalytic evaluations revealed an essential interplay among these parameters and the photoreactivity of the resulting materials. Beyond basic considerations, such as spectral absorption and crystallinity, the material's lattice symmetry has a significant impact on photoreactivity. We anticipate that the structure-performance relationships developed will provide a robust rule of thumb for designing COF-based photocatalysts.

INTRODUCTION

Harnessing the energy of light to make and break chemical bonds usually involves semiconducting photocatalysts, with titanium dioxide being the benchmark.[1–4] Recently, organic photoredox catalysts have been acknowledged in a myriad of chemical transformations, due to their diverse synthetic modularity, as promising for the discovery and optimization of new reaction routes.[5,6] While impressive advances have been achieved, engineering the optical properties to improve efficiency through the direct functionalization of chromophore moieties is often cumbersome and synthetically challenging. In addition, the molecular photoredox catalysts often suffer from photobleaching, compromising their long-term stable outputs.[7] Alleviating the deactivation and enhancing control over the conversion of light into chemical energy are essential in furthering this technology.[8–18]

Covalent organic frameworks (COFs) are molecular "Legos" that enable the clear-cut integration of organic struts into extended crystalline frameworks,[19–27] tailor-made for use in a wide variety of applications such as catalysis,[28–31] environmental remediation,[32–34] and bio-related applications,[35–37] to name a few.[38–40] In terms of light-response properties, two-dimensional (2D) COFs offer unparalleled advantages.[41–53] The modularity that comes with the use of COFs offers the ability to incorporate chromophore struts from the expansive list of organic molecular photoredox catalysts into 2D extended polygons. The resulting close face-on-oriented packing

Progress and Potential

Harnessing the energy of light to trigger chemical reactions has attracted considerable interest. Development of efficient photosensitizers through direct molecule engineering is often synthetically challenging. Advancements in reticular chemistry have enhanced our ability to design and develop materials tailor-made for use in a wide variety of applications. Here, we demonstrate how the two-dimensional covalent organic frameworks (COFs) display the appropriate combination of properties to serve as a scaffold for photocatalyst design. We conducted a series of comparative studies detailing the design principles for the achievement of highly efficient photocatalysts. These descriptors allow us to establish the first relationships between the composition, crystallinity, lattice symmetry, and photoreactivity for this class of materials. We anticipate that our work will guide future efforts to make COFs suitable for practical photocatalytic transformations and related applications.
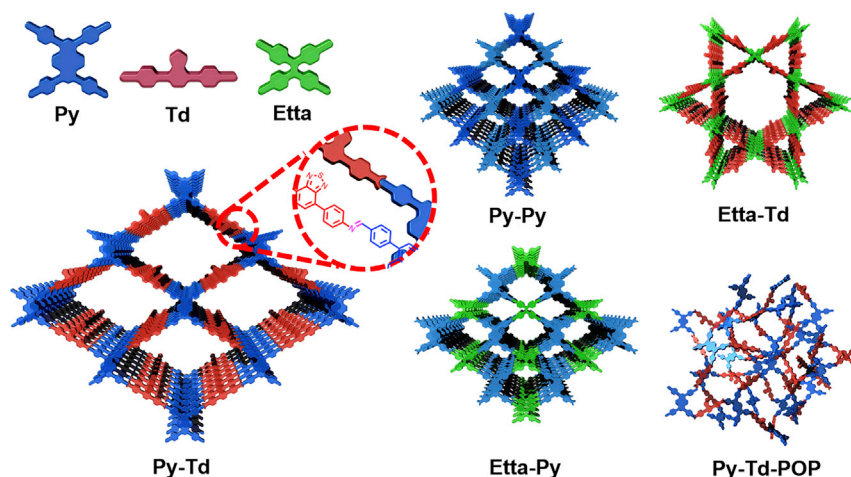
Figure 1. Structure of the Struts and the Corresponding Synthesized Materials Built with Amine Bonds

leads to significant electronic overlap, providing another possible path for migration of charge carriers and excitations in addition to transfer within the covalent sheets. Given these factors, COFs are expected to be an enticing scaffold with colligative properties that are distinct from small molecules or randomly bonded networks to optimize the photosensitizers' ability to generate reactive intermediates. The periodically ordered charge-transporting networks give opportunities for developing a fundamental understanding of the relationships among chemical structure, lattice symmetry, and light-induced processes, ultimately obtaining design rules for the creation of efficient photocatalysts. Additionally, the heterogeneous nature of the COFs allows for an increase in operational ability and easy separation, together with ready incorporation into continuous-flow systems. Furthermore, the formed polymer matrices act as an effective oxygen diffusion barrier, resulting in enhanced resistance against photobleaching.

Previous efforts toward the synthesis of COF-based photocatalysts were mainly focused on the direct modification of a specific fragment, such as the chromophore strut and type of linkage, which fails to provide a convincing case for how the periodically conjugated 2D framework structure allows for the additional optimization of the optical properties.[54,55] Given the high degree of electronic communication throughout the framework, it is envisaged that we can manage the light-absorption and charge-separation properties of the resulting COFs by matching the electronic properties and geometry of the organic struts. In this contribution, we started from three established chromophores (pyrene, tetraphenylethylene, and thiadiazole; Figure 1). Based on these struts, a set of porous materials with different levels of crystallinity and topology were synthesized to investigate the factors governing the photoreactivity (see detailed synthetic scheme in Supplemental Experimental Procedures). To establish such correlations, we conducted comparative studies by individually varying these parameters. We demonstrated that there is an important interplay between composition, crystallinity, and topology on the reactivity of the resultant photocatalyst. It is no longer possible to design photocatalysts based purely on their optical absorption, which has been the dominant paradigm to date. This contribution represents a study of direct electronic structure-performance relationships of porous organic photosensitizers, offering valuable insights into the design of high-efficiency photocatalysts and highlighting COFs as a bespoke platform for numerous applications.

[1]Key Lab of Applied Chemistry of Zhejiang Province, Zhejiang University, Hangzhou 310028, China

[2]College of Chemical and Biological Engineering, Zhejiang University, Hangzhou 310027, China

[3]Department of Chemistry, University of South Florida, 4202 East Fowler Avenue, Tampa, FL 33620, USA

[4]State Key Laboratory of Magnetic Resonance and Atomic and Molecular Physics, Wuhan Institute of Physics and Mathematics, Chinese Academy of Sciences, Wuhan 430071, China

[5]Department of Chemistry and Biochemistry, North Dakota State University, 1340 Administration Avenue, Fargo, ND 58102, USA

[6]Lead Contact

*Correspondence: sunqichs@zju.edu.cn (Q.S.), sqma@usf.edu (S.M.), fsxiao@zju.edu.cn (F.-S.X.)

https://doi.org/10.1016/j.matt.2019.10.026

RESULTS

Material Synthesis

To implement this strategy, we selected the Schiff base reaction for constructing photoactive COFs. COFs built with imine bonds have not only been proven to synthesize materials with high crystallinity and chemical stability toward a wide range of conditions but have also shown excellent geometrical and functional compatibility, thereby offering the opportunity for optimizing their photophysical properties. As a proof-of-concept study, we chose three well-known chromophore struts for the construction of photoactive materials to elucidate the underlying structure-reactivity relationship. Pairing the tetradentate 1,3,6,8-tetrakis(4-aminophenyl)pyrene, $Py(NH_2)_4$, with 1,3,6,8-tetrakis(4-formylphenyl)pyrene, $Py(CHO)_4$, gave rise to the Py-Py COF, which is anticipated to yield the minimum donor-acceptor contrast, stemming mainly from the slightly polarized, electron-accepting imine bond. Switching from pairing two of the same chromophore struts, two different tetradentate struts, $Py(CHO)_4$ and 4,4′,4″,4‴-(ethene-1,1,2,2-tetrayl)tetraaniline (Etta), were combined, with the fabricated COF named Etta-Py. To further increase the charge transfer in the resulting COFs, we introduced an electron-deficient heterocycle moiety, thiadiazole (Td), into the COF synthesis which, teaming up with $Py(CHO)_4$, yielded the Py-Td COF. To scrutinize the impact of lattice symmetry on the performance of COFs, except for four-arm cores, we synthesized a three-arm core COF by pairing Etta with Td. Moreover, to investigate the role of long-range order, we prepared the amorphous counterpart of the Py-Td COF (Py-Td-POP) for comparison (Figure 1).

Physicochemical Characterization and Local Structure Analysis

These materials were synthesized under acid-catalyzed solvothermal conditions. The formation of the imine linkage in all synthesized COFs was verified by Fourier transform infrared (FTIR) spectroscopy, whereby we observed the appearance of characteristic C=N stretching modes at 1,620 cm^{-1}, as well as a complete disappearance of N–H stretching of the primary amines (3,370–3,210 cm^{-1}) and aldehyde band (2,800–2,720 cm^{-1}) from the monomers. Solid-state ^{13}C nuclear magnetic resonance (NMR) spectra showing a peak at around 160 ppm, in line with the C=N bond, provided additional evidence of the formation of the imine linkage (Figures S1, S2, S6, S7, S12, S13, S18, and S19).

The powder X-ray diffraction (PXRD) pattern of Py-Td contains several prominent diffraction peaks, indicating the high crystallinity of the material. The identification of the resulting structure was achieved through a comparison of structures modeled using Materials Studio (Figure 2A). The corresponding powder patterns were simulated based on the optimized *CM* symmetric structure model and compared with the experimentally obtained data, which showed good agreement with each other (Figure 2B). Pawley refinement of the PXRD pattern was carried out for full profile fitting against the proposed model of AA packing, which resulted in good agreement factors (R_{WP} = 2.1 after convergence) and reasonable profile differences (Figure S3). We ascribe the slight shifts of the experimental PXRD patterns against the simulated ones to the sample displacement error that is in reflection mode; if the sample height is different from the focal plane, peak positions will be shifted. The morphology of Py-Td was examined using scanning electron microscopy (SEM), with the majority showing pill-shaped aggregates of irregular polyhedral particles, suggestive of phase purity (Figures 2A [inset] and S4). Nitrogen sorption isotherms of Py-Td collected at 77 K revealed that it formed a porous structure with distinguishable mesopores. The Brunauer-Emmett-Teller (BET) surface area and pore volume were
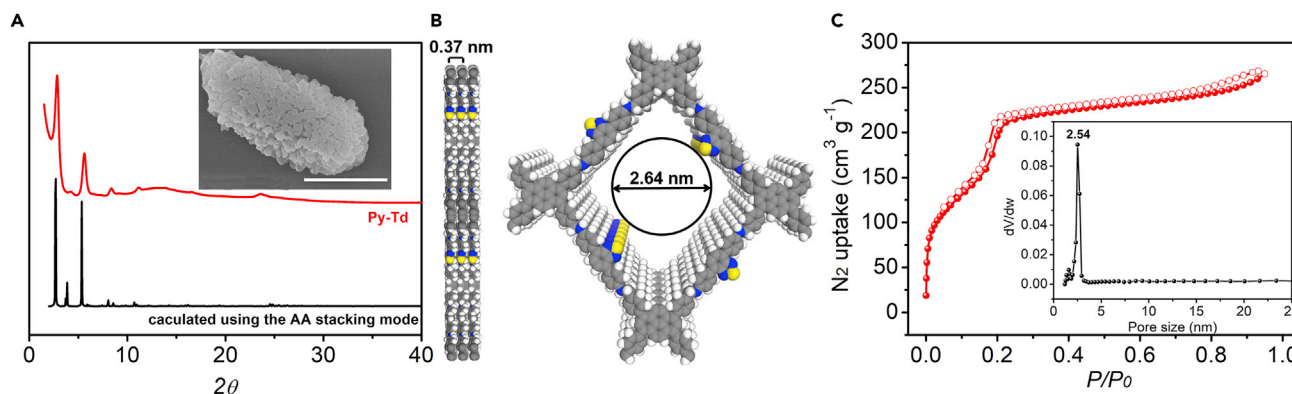
Figure 2. Characterization of the Py-Td COF

(A) Experimental and calculated PXRD patterns. Inset: SEM image of Py-Td (scale bar, 1 μm).

(B) Graphic view of AA-stacking mode of Py-Td (gray, C; blue, N; yellow, S; white, H).

(C) N_2 sorption isotherms collected at 77 K. Inset: corresponding pore-size distribution of Py-Td derived from the NLDFT method.

See also Figures S1–S5.

estimated to be 672 m^2 g^{-1} and 0.40 cm^3 g^{-1}, respectively (Figure 2C). Based on nonlocal density functional theory (NLDFT), a narrow pore-size distribution centering at 2.54 nm was obtained, matching well with the predicted values for the geometry of an AA eclipsed framework (2.64 nm). The Py-Td COF can retain its crystallinity after the treatment of both acid (1 M HCl) and base (3 M NaOH) aqueous solutions for 24 h (Figure S5).

The Py-Py and Etta-Py COFs are also highly crystalline frameworks, as established by the intense reflections in the PXRD patterns. Structure elucidation revealed that these two COFs shared the same symmetry of *P2/m* with a pseudo-quadratic geometry similar to that of the Py-Td COF. Both samples showed reversible type I isotherms, indicative of the uniform microporous structure of these materials. Fitting these isotherms gave BET surface areas of 958 and 1,858 m^2 g^{-1} and pore-size distributions peaking at 1.50 and 1.30 nm for Py-Py and Etta-Py, respectively. With respect to the Etta-Td COF, the PXRD analysis revealed that it crystallized in the *P6m* space group with a structure that was in excellent agreement with the proposed AA-stacking mode of a dual-pore Kagome structure. Derived from N_2 sorption isotherms, the calculated BET surface area for this material was 749 m^2 g^{-1} with two different pore sizes predominantly distributed at ca. 3.8 and 1.5 nm, assignable to the hexagonal mesopores and triangular micropores, respectively. For the detailed characterization of Py-Py, Etta-Py, and Etta-Td, see Figures S6–S23 and Table S1.

Optical Property Investigation

Given that a material's optical band-gap and energy-level alignment have profound consequences on its photoreactivity, these properties of the resulting COFs were investigated through a combination of UV-visible (UV-vis) spectroscopy, Mott-Schottky analysis, cyclic voltammetry (CV) measurement, and density functional theory (DFT) calculation for cross-validation. To examine optical absorption profiles, we carried out UV-vis spectroscopy measurements, which showed distinct differences among these COFs. Etta-Py exhibited an absorption maximum at 470 nm with an absorbance edge at around 563 nm. In comparison, the spectra of the other three COFs are extended to broader regions, with a comparable maximum absorption peak of 514 nm; the absorption onsets are red-shifted in the order of Etta-Td > Py-Td > Py-Py (Figure 3A). The appearance of such differences in the visible-light
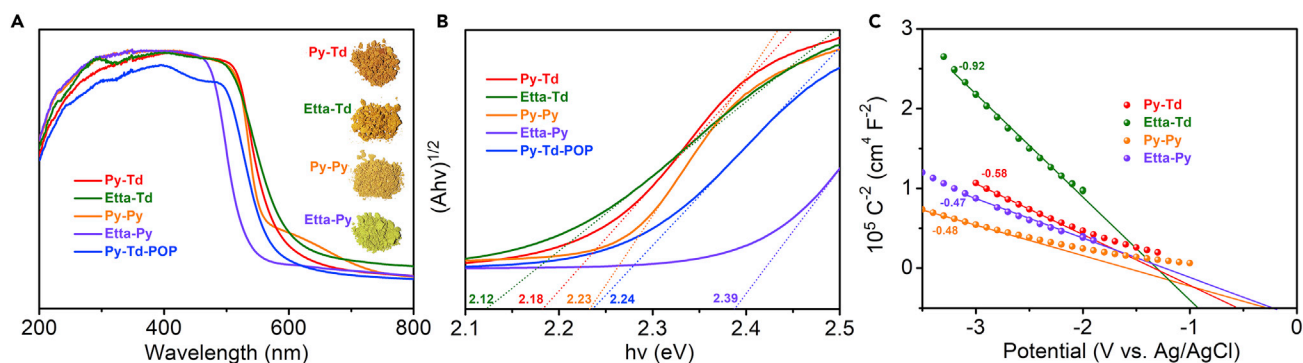
Figure 3. Optical Property Investigation
(A) Normalized UV-vis absorption spectra. Inset: digital images of (from top to bottom) Py-Td, Etta-Td, Py-Py, and Etta-Py COFs.
(B) Tauc plots.
(C) Mott-Schottky plots in 0.2 M Na_2SO_4 aqueous solution at 1,000 Hz.
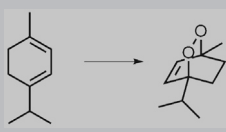See also Figures S6–S23.

region is also indicated by colors ranging from yellow to brick red (Figure 3A, inset), inferring that the electronic band structures around the band gaps of these materials are significantly different (Figure 3B). Based on the equation $(Ah\nu)^2 = \alpha(h\nu - E_g)$, the optical band gaps calculated from the plots are 2.39, 2.23, 2.18, and 2.12 eV for Etta-Py, Py-Py, Py-Td, and Etta-Td, respectively, revealing that the incorporation of the Td moieties helps to narrow the band gap. By contrast, Py-Td-POP, an amorphous analog of the Py-Td COF, showed an abridged visible-region absorption and an increased band gap to about 2.24 eV, probably as a result of the limited extension of conjugation due to the twisted and disordered structures.[56]

To gain detailed information about the energy-level alignment of the COFs, we performed Mott-Schottky electrochemical measurements (Figure 3C). All the tested materials gave negative slopes of the Mott-Schottky plots, suggestive of a p-type semiconductor behavior. The flat band position values of these COFs calculated via the Mott-Schottky equation at $1/C^2 = 0$ are −0.58, −0.92, −0.48, and −0.47 V versus Ag/AgCl (i.e., −0.58 V, −0.34 V versus normal hydrogen electrode [NHE]); thus, the corresponding conductor bands are estimated to be −0.34 V, −0.68 V, −0.24 V, and −0.23 V versus NHE for the Py-Td, Etta-Td, Py-Py, and Etta-Py COFs, respectively. The valence band positions at 1.84, 1.44, 1.99, and 2.16 V versus the NHE for Py-Td, Etta-Td, Py-Py, and Etta-Py could thus be derived from the optical band gap. We further determined the LUMO (lowest unoccupied molecular orbital) and HOMO (highest occupied molecular orbital) energy levels of these materials, corresponding to their conduction and valence band edges, by using CV measurement that revealed a consistent trend with the Mott-Schottky tests (Figures S24 and S25). Furthermore, DFT calculations of the fragmental structures of the COF networks verified that the energy band gaps and energy alignment follow the same trend as those obtained from the experiments (Figure S26 and Table S2).

Catalytic Performance Evaluation
We sought to investigate the photoreactivity of these materials. Among the developed photocatalytic transformations, molecular oxygen (O_2) involving oxidation reactions has been of great interest, whereby active oxygen species can be generated via the energy or electron-transfer pathway from photocatalyst to O_2. Given the oxidizing and electrophilic properties of $^1O_2$, this species has been under scrutiny and has proved useful in a variety of applications.[57] These materials were thus

Table 1. Catalytic Evaluation of α-Terpinene into Ascaridole over Various Photosensitizers[a]

Entry	Catalyst	Light	Heat	Yield (%)[b]
1	–	+	–	<1
2	Py-Td	–	–	<1
3	Py-Td	–	+	<1
4	Py-Td	+	–	84
5	Py-Td-POP	+	–	51
6	Py-Py	+	–	24
7	Etta-Td	+	–	52
8	Etta-Py	+	–	29
9	thiadiazole	+	–	11
10	tetraphenylethylene	+	–	4
11	tetraphenylpyrene	+	–	26

[a]Standard reactions were conducted with 1 mmol of α-terpinene and 5 mg of photosensitizer, in 5 mL of $CHCl_3$ at room temperature under blue LED irradiation with a power of 10 W/m (total 10 W) for 3 h.
[b]Yields were determined by ^1H NMR analysis.

initially examined as triplet photosensitizers in the $^1O_2$ production. To evaluate the efficiency in photogenerated $^1O_2$, we tested their performances in the Alder-Ene reaction with α-terpinene as a trapping reagent, as this only proceeds with $^1O_2$, therefore facilitating comparisons.[58] The production of $^1O_2$ over various materials was monitored by calculating the conversion of α-terpinene into ascaridole (Table 1). To confirm the $^1O_2$ generation mechanism, we first conducted three control experiments as follows: (1) in the absence of any photosensitizer; (2) in the dark and in the presence of photosensitizing material; and (3) in the dark and with heating of the COFs. Each of these controls showed no ascaridole yield, which is, therefore, indicative of no $^1O_2$ generated under the aforementioned conditions (Table 1, entries 1–3). An 84% conversion of α-terpinene to ascaridole was detected after 3 h of irradiation in the presence of Py-Td under the 420-nm light-emitting diode (LED) modules (Table 1, entry 4). Under otherwise identical conditions, its amorphous counterpart, Py-Td-POP (BET: 477 $m^2 g^{-1}$; Figure S27), afforded an ascaridole yield of 51%, which is only around 60% as much as that achieved by using Py-Td (Table 1, entry 5). Given the same chemical composition, their discrepancy in efficiency could have stemmed from their structural differences, wherein the COF skeleton with extended planarity is proved to increase the light absorbability. Moreover, crystalline structures with fewer defects could suppress the recombination of photogenerated electron and hole pairs, thereby highlighting the uniqueness of COFs for photocatalysis. Comparisons of the $^1O_2$ generation efficiency of Py-Td with that of other COF materials, including Py-Py, Etta-Py, and Etta-Td, indicate that the efficiency for Py-Td is between 1.6- and 3.5-fold greater (Table 1, entries 6–8). Considering that all of these COFs are connected by the same imine linkage and paired by two of the three struts, the vast disparities with regard to the photoactive capabilities of these COFs should be more than merely a specific strut. To experimentally prove this, we evaluated the performance of all the struts involved in the COF syntheses, resulting in activities inferior to or comparable with the COFs (Table 1, entries 9–11). Taken together, the divergent outcomes of these COFs may not be pinpointed to a single
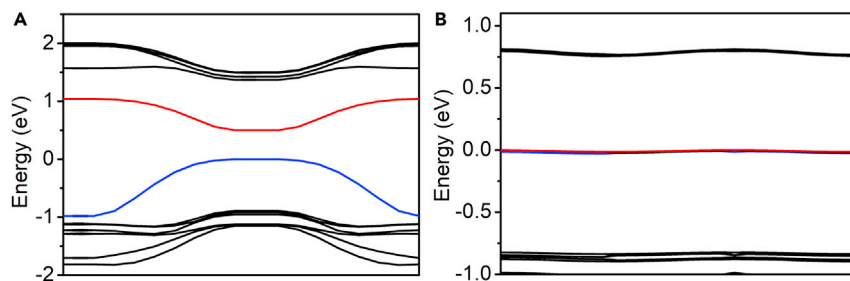
Figure 4. Band-Structure Profiles
(A and B) Band-structure profiles of (A) Py-Td and (B) Etta-Td.

factor change but rather considered a result of a complex interplay of several aspects. An increase in photoabsorption and proper energy-level alignment can be used to explain the superior performance of Py-Td in comparison with Etta-Py and Py-Py. However, in the cases of Py-Td and Etta-Td, only a very weak correlation between the catalytic performance and the photoproperties could be established, given that Etta-Td with a broader photoabsorption range and lower LUMO energy level than Py-Td offered an inferior result. Therefore, their activity discrepancy may be ascribed to their differences in charge-carrier lifetime, another critical parameter for an efficient photocatalyst. Indeed, computational studies reveal that Etta-Py with *P6m* symmetry exhibits a nearly flat and overlapped top valence band, resulting in high charge-carrier effective masses.[59] In contrast, the top valence band of Py-Td with *C2/m* symmetry displays a significant dispersion, giving superior charge-carrier mobility (Figure 4). These results are in good agreement with the recent theoretical prediction associated with symmetry-electronic property relationships for 2D π-conjugated materials.[59] To further validate this experimentally, we evaluated excited-state lifetimes of Py-Td and Etta-Td by time-correlated single-photon counting (TCSPC) spectroscopy in the air at 298 K, verifying that Py-Td showed much longer decay lifetimes than Etta-Td (Figure 5A).

Considering the efficiency in the generation of $^1O_2$, this prompted investigations into the potential of these materials in other chemical transformations. Among the developed catalytic reactions that involved triplet photosensitizers, we were interested in the photooxidation of organic sulfides. Given the superior performance, Py-Td was our choice for detailed investigations. The reactivity of Py-Td under visible light was investigated by the photooxidation of thioanisole.[60] A full conversion of thioanisole to the desired monooxidized product methyl phenyl sulfoxide with a selectivity of 96% was obtained (Table S3, entry 1). Photooxygenation of sulfides involves either an energy-transfer process, whereby $^1O_2$ reacts with sulfides to afford the sulfoxides, or an electron-transfer process, whereby a superoxide radical ($O_2^{\bullet-}$) acts as an electron mediator in the photoredox cycle. To detect the generated reactive oxygen species by Py-Td, we carried out electron paramagnetic resonance (EPR) measurements. Both EPR signals for $^1O_2$ and $O_2^{\bullet-}$ were unequivocally detected when 2,2,6,6-tetra-methyl-1-piperidine (TEMP) and 5,5′-dimethyl-1-pyrroline *N*-oxide (DMPO), respectively, were used as trapping agents (Figures 5B and S28).

To obtain more information about the reaction pathway, we investigated the role of each reactive oxygen species. When *p*-benzoquinone, an $O_2^{\bullet-}$ scavenger, was introduced to the reaction system, the conversion of thioanisole decreased to 72%, indicative of the role of $O_2^{\bullet-}$. To identify the role of $^1O_2$, we introduced the singlet oxygen scavenger, sodium azide (NaN$_3$), to the reaction system, and the conversion of thioanisole decreased slightly to 93%. Using ethene-1,1,2,2-tetracarbonitrile as a
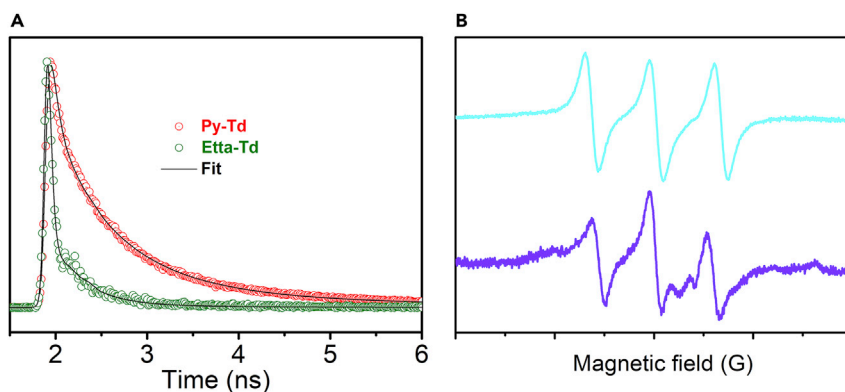
Figure 5. Excited-State Lifetime and Reactive Oxygen Species Investigation
(A) Time-correlated single-photon counting profiles of Py-Td and Etta-Td.
(B) EPR spectra of CH_3CN solutions of DMPO (violet) and TEMP (cyan) in the presence of Py-Td after irradiation under visible light.
See also Figures S25 and S26.

hole scavenger, only 7% of the conversion was measured. A sharply decreased yield (8%) was also observed with 10H-phenothiazine as an electron scavenger (Table S3).[61,62] Based on these results, a plausible reaction mechanism for the Py-Td catalyzed the oxidation of sulfides is proposed. The excited Py-Td* experiences an oxidative quenching process by the transfer of electrons to O_2. Through a redox reaction, the sulfides are oxidized by the holes in the valence band of the photosensitizer with the simultaneous regeneration of Py-Td and formation of sulfide radical cation, which is further oxidized by $O_2^{\bullet-}$ or $^1O_2$ to afford the desired products.

To expand the applicability of this material, we carried out experiments in batch under natural sunlight irradiation as an alternative to the Xe lamp. Full conversion was achieved within 30 min in the presence of Py-Td. Using sunlight, along with superior performance, we were able to validate the efficiency of the Py-Td COF, thus implying its potential for low-environmental-impact transformations.

Catalytic Performance Evaluation in a Continuous-Flow Reactor
The fast reaction rate together with the stability of COFs encouraged us to adopt a simple continuous-flow system, which offers facile automation and ready control over reaction parameters. Furthermore, concerns associated with photon penetration depth and overirradiation under batch conditions can be avoided. A continuous-flow experiment was then conducted using Py-Td with the experimental setup described in Figure 6. A full conversion of thioanisole after a single pass of the 1-mL solution of thioanisole (50 µL in 20 mL of acetonitrile) was observed, prompting further investigations to determine the long-term stability of Py-Td. To examine this, we allowed a continuous stream of the thioanisole solution to pass through the column, taking measurements at 1-h intervals. No decrease in the conversion rate was observed after 50 measurements (Figure 6). To further validate the stability of Py-Td under reaction conditions, we evaluated its recyclability in the photooxidation of thioanisole by monitoring the performance over five consecutive runs, showing that both conversion and selectivity were maintained, indicating its robust structure, which was further evidenced by its retained PXRD pattern (Figures S29 and S30). The Py-Td COF is also chemically stable, as supported by the negligible difference in the solid-state ^{13}C NMR spectra between the fresh synthesized Py-Td and the one that has been used five times (Figure S30).
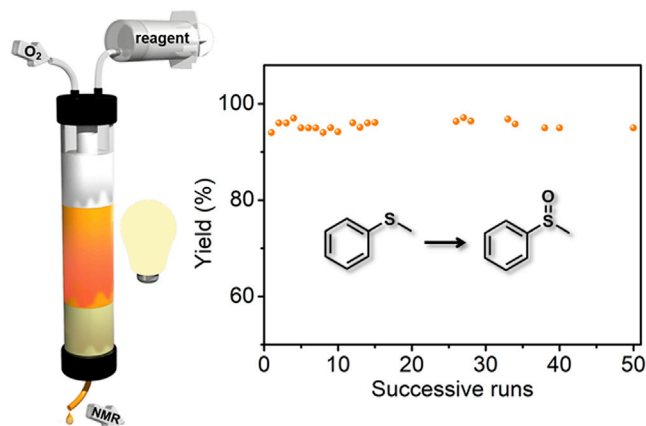
Figure 6. Reaction under Continuous-Flow Conditions

Schematic illustration of the column photoreactor in a continuous-flow system. The porous polymers are inserted into the gas column. General reaction conditions: Py-Td (20 mg), flow rate of thioanisole in acetonitrile (1 mL h^{-1}), O$_2$ (1 mL min^{-1}), room temperature, and Xe lamp.

Scope of Investigation

To explore the versatility of the Py-Td catalyst, we examined a number of sulfide derivatives. Various aryl sulfide substrates bearing chlorine, fluorine, methoxy, and methyl functionalities could be selectively oxidized with moderate to high conversions (Table S4). Encouraged by these results, we proceeded to test the applicability of Py-Td for sulfur mustard simulant oxidation. As one of the most broadly used and notorious chemical weapons, sulfur mustard can cause grievous skin blisters and irritation to the respiratory system, or even death at high doses.[63] The selective oxidative detoxification of sulfur mustard to sulfoxide is a promising route. In this context, the capability of Py-Td in the oxidation of a sulfur mustard simulant 2-chloroethyl ethyl sulfide (CEES) was evaluated, affording full conversion within 1 h and thereby exhibiting great potential for rapidly and highly selectively detoxifying sulfur mustard (Table S4, entry 6).

Considering the results mentioned above, we proceeded to integrate Py-Td with protective fabrics to combine the self-detoxifying properties of the COF with the air permeation of textiles. To target this, we chose nylon-66 fabric because of its chemical resistance and mechanical strength. To increase the affinity between the substrate and the COF for potential application in process-intensive conditions, we first modified the fabric with polydopamine, followed by a bottom-up synthetic pathway, by submerging it into the system for COF synthesis. The SEM images indicate the successful deposition of the Py-Td COF crystals on it (Figures S31 and S32). The composite exhibited excellent performance regarding the oxidation of CEES with full conversion within 1 h (0.5 µL of CEES in 1 mL of acetonitrile) (Figure 7).

DISCUSSION

The foregoing results detail design principles targeting highly efficient photocatalysts: (1) electronic properties of the paired struts—the combination of donor-acceptor charge transfer imparts a marked band-gap narrowing for the resulting material; (2) crystallinity—the unique structure of 2D COFs can increase the photoabsorption capability and exciton dissociation yields; (3) lattice symmetry—four-arm core COFs are superior to three-arm core COFs in terms of charge-carrier lifetime. These descriptors have allowed us to establish the first relationships between the
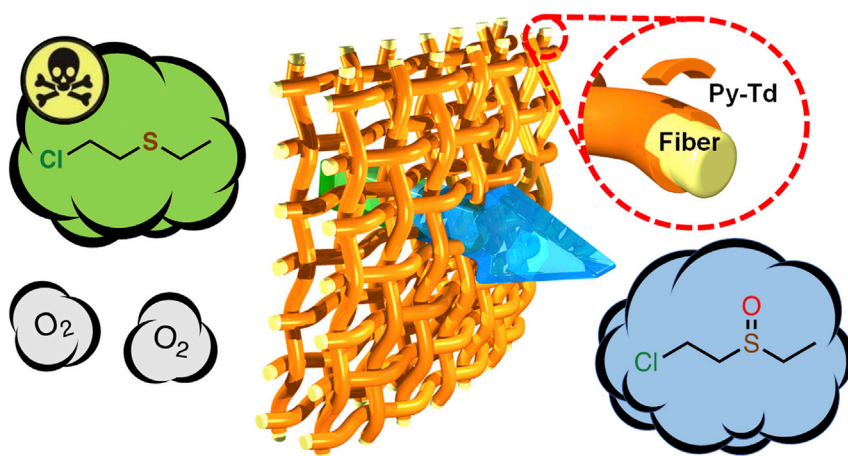
Figure 7. Schematic Illustration of the Preparation of Py-Td-Coated Fabric for Photooxidation of CEES

See also Figures S31 and S32.

crystallinity, lattice symmetry, and property for this class of materials. With the achieved material, the catalysis can be performed under sunlight or in a continuous-flow reactor, as well as through integration with substrates, showing great potential in practical applications. We anticipate that the tunability of COF systems in terms of both composition and topology will promote further opportunities for a wide array of catalytic transformations and related applications.

EXPERIMENTAL PROCEDURES

Materials

Commercially available reagents were purchased in high purity and used without purification. The purity of the monomers used for COF synthesis was determined by NMR analyses (Figure S33).

Characterization

PXRD data were collected on a Bruker AXS D8 Advance A25 Powder X-ray diffractometer (40 kV, 40 mA) using Cu-Kα (λ = 1.5406 Å) radiation. The gas adsorption isotherms were collected on a surface area analyzer, ASAP 2020. The N_2 sorption isotherms were measured at 77 K using a liquid N_2 bath. SEM images were collected using a Hitachi SU 8010 or SU 1510. Infrared spectra were recorded on a Nicolet Impact 410 FTIR spectrometer. ^{1}H NMR spectra were recorded on a Bruker Avance-400 (400 MHz) spectrometer. Chemical shifts are expressed in ppm downfield from tetramethylsilane at δ = 0 ppm, and J values are given in Hz. ^{13}C (100.5 MHz) cross-polarization magic-angle spinning was recorded on a Varian Infinity Plus 400 spectrometer equipped with a magic-angle spin probe in a 4-mm ZrO_2 rotor. UV-vis spectra were measured using Shimadzu UV-3600 UV-vis spectrophotometer with an integration sphere setup. TCSPC measurements were performed on a LifeSpec-II fluorescence spectrometer employing an EPL485 pulsed laser diode and a Hamamatsu H5773-04 photomultiplier.

SUPPLEMENTAL INFORMATION

Supplemental Information can be found online at https://doi.org/10.1016/j.matt.2019.10.026.

REFERENCES

1. Asahi, R., Morikawa, T., Ohwaki, T., Aoki, K., and Taga, A.Y. (2001). Visible-light photocatalysis in nitrogen-doped titanium oxides. Science *293*, 269–271.

2. Lang, X., Chen, X., and Zhao, J. (2014). Heterogeneous visible light photocatalysis for selective organic transformations. Chem. Soc. Rev. *43*, 473–486.

3. Yoon, T.P., Ischay, M.A., and Du, J. (2010). Visible light photocatalysis as a greener approach to photochemical synthesis. Nat. Chem. *2*, 527–532.

4. Wang, X., Zhang, L., Chen, Z., Hu, J., Li, S., Wang, Z., Liu, J., and Wang, X. (2014). Semiconductor heterojunction photocatalysts: design, construction, and photocatalytic performances. Chem. Soc. Rev. *43*, 5234–5244.

5. Romero, N.A., and Nicewicz, D.A. (2016). Organic photoredox catalysis. Chem. Rev. *116*, 10075–10166.

6. McAtee, R.C., McClain, E.J., and Stephenson, C.R.J. (2019). Illuminating photoredox catalysis. Trends Chem. *1*, 111–125.

7. Liang, H.-P., Chen, Q., and Han, B.-H. (2018). Cationic polycarbazole networks as visible-light heterogeneous photocatalysts for oxidative organic transformations. ACS Catal. *8*, 5313–5322.

8. Zhang, G., Lan, Z.-A., and Wang, X. (2016). Conjugated polymers: catalysts for photocatalytic hydrogen evolution. Angew. Chem. Int. Ed. *55*, 15712–15727.

9. Ma, L., Liu, Y., Liu, Y., Jiang, S., Li, P., Hao, Y., Shao, P., Yin, A., Feng, X., and Wang, B. (2019). Ferrocene-linkage-facilitated charge separation in conjugated microporous polymers. Angew. Chem. Int. Ed. *58*, 4221–4226.

10. Zhang, K., Kopetzki, D., Seeberger, P.H., Antonietti, M., and Vilela, F. (2013). Surface area control and photocatalytic activity of conjugated microporous poly(benzothiadiazole) networks. Angew. Chem. Int. Ed. *52*, 1432–1436.

11. Wu, W., Xu, S., Qi, G., Zhu, H., Hu, F., Liu, Z., Zhang, D., and Liu, B. (2019). A cross-linked conjugated polymer photosensitizer enables efficient sunlight-induced photooxidation. Angew. Chem. Int. Ed. *58*, 3062–3066.

12. Li, L., Cai, Z., Wu, W.-Y., Zhang, N., Chen, L.X., and Yu, L. (2016). Rational design of porous conjugated polymers and roles of residual palladium for photocatalytic hydrogen production. J. Am. Chem. Soc. *138*, 7681–7686.

13. Sprick, R.S., Jiang, J.-X., Bonillo, B., Ren, S., Ratvijitvech, T., Guiglion, P., Zwijnenburg, M.A., Adams, D.J., and Cooper, A.I. (2015). Tunable organic photocatalysts for visible-light-driven hydrogen evolution. J. Am. Chem. Soc. *137*, 3265–3270.

14. Zhang, T., and Lin, W. (2014). Metal-organic frameworks for artificial photosynthesis and photocatalysis. Chem. Soc. Rev. *43*, 5982–5993.

15. Li, R., Byun, J., Huang, W., Ayed, C., Wang, L., and Zhang, K.A.I. (2018). Poly(benzothiadiazoles) and their derivatives as heterogeneous photocatalysts for visible-light-driven chemical transformations. ACS Catal. *8*, 4735–4750.

16. Yu, X., Yang, Z., Qiu, B., Guo, S., Yang, P., Yu, B., Zhang, H., Zhao, Y., Yang, X., Han, B., and Liu, Z. (2019). Eosin Y-functionalized conjugated organic polymers for visible light-driven CO₂ reduction with H₂O to CO with high efficiency. Angew. Chem. Int. Ed. *58*, 632–636.

17. Sun, D., Jang, S., Yim, S.-J., Ye, L., and Kim, D.-P. (2018). Metal doped core-shell metal-organic frameworks@covalent organic

frameworks (MOFs@COFs) hybrids as a novel photocatalytic platform. Adv. Funct. Mater. *28*, 1707110.

18. Xiao, J.-D., and Jiang, H.-L. (2019). Metal-organic frameworks for photocatalysis and photothermal catalysis. Acc. Chem. Res. *52*, 356–366.

19. Côté, A.P., Benin, A.I., Ockwig, N.W., O'Keeffe, M., Matzger, A.J., and Yaghi, O.M. (2005). Porous, crystalline, covalent organic frameworks. Science *310*, 1166–1170.

20. Feng, X., Ding, X., and Jiang, D. (2012). Covalent organic frameworks. Chem. Soc. Rev. *41*, 6010–6022.

21. Ding, S.-Y., and Wang, W. (2013). Covalent organic frameworks (COFs): from design to applications. Chem. Soc. Rev. *42*, 548–568.

22. Song, Y., Sun, Q., Aguila, B., and Ma, S. (2019). Opportunities of covalent organic frameworks for advanced applications. Adv. Sci. *8*, 1801410.

23. Bisbey, R.P., and Dichtel, W.R. (2017). Covalent organic frameworks as a platform for multidimensional polymerization. ACS Cent. Sci. *3*, 533–543.

24. Zhou, T.-Y., Xu, S.-Q., Wen, Q., Pang, Z.-F., and Zhao, X. (2014). One-step construction of two different kinds of pores in a 2D covalent organic framework. J. Am. Chem. Soc. *136*, 15885–15888.

25. Kandambeth, S., Dey, K., and Banerjee, R. (2019). Covalent organic frameworks: chemistry beyond the structure. J. Am. Chem. Soc. *141*, 1807–1822.

26. Lohse, M.S., and Bein, T. (2018). Covalent organic frameworks: structures, synthesis, and applications. Adv. Funct. Mater. *28*, 170553.

27. Jin, Y., Hu, Y., and Zhang, W. (2017). Tessellated multiparous two-dimensional

covalent organic frameworks. Nat. Rev. Chem. *1*, https://doi.org/10.1038/s41570-017-0056.

28. Sun, Q., Aguila, B., Perman, J.A., Nguyen, N., and Ma, S. (2016). Flexibility matters: cooperative active sites in covalent organic framework and threaded ionic polymer. J. Am. Chem. Soc. *138*, 15790–15796.

29. Wang, X., Han, X., Zhang, J., Wu, X., Liu, Y., and Cui, Y. (2016). Homochiral 2D porous covalent organic frameworks for heterogeneous asymmetric catalysis J. Am. Chem. Soc. *138*, 12332–12335.

30. Lu, S., Hu, Y., Wan, S., McCaffrey, R., Jin, Y., Gu, H., and Zhang, W. (2017). Synthesis of ultrafine and highly dispersed metal nanoparticles confined in a thioether-containing covalent organic framework and their catalytic applications. J. Am. Chem. Soc. *139*, 17082–17088.

31. Liu, H., Chu, J., Yin, Z., Cai, X., Zhuang, L., and Deng, H. (2018). Covalent organic frameworks linked by amine bonding for concerted electrochemical reduction of CO_2. Chem *4*, 1696–1709.

32. Sun, Q., Aguila, B., Perman, J., Earl, L., Abney, C., Cheng, Y., Wei, H., Nguyen, N., Wojtas, L., and Ma, S. (2017). Postsynthetically modified covalent organic frameworks for efficient and effective mercury removal. J. Am. Chem. Soc. *139*, 2786–2793.

33. Huang, N., Zhai, L., Xu, H., and Jiang, D. (2017). Stable covalent organic frameworks for exceptional mercury removal from aqueous solutions. J. Am. Chem. Soc. *139*, 2428–2434.

34. Li, Z., Li, H., Guan, X., Tang, J., Yusran, Y., Li, Z., Xue, M., Fang, Q., Yan, Y., Valtchev, V., and Qiu, S. (2017). Three-dimensional ionic covalent organic frameworks for rapid, reversible, and selective ion exchange. J. Am. Chem. Soc. *139*, 17771–17774.

35. Kandambeth, S., Venkatesh, V., Shinde, D.B., Kumari, S., Halder, A., Verma, S., and Banerjee, R. (2015). Self-templated chemically stable hollow spherical covalent organic framework. Nat. Commun. *6*, 6786.

36. Peng, Y., Huang, Y., Zhu, Y., Chen, B., Wang, L., Lai, Z., Zhang, Z., Zhao, M., Tan, C., Yang, N., et al. (2017). Ultrathin two-dimensional covalent organic framework nanosheets: preparation and application in highly sensitive and selective DNA detection. J. Am. Chem. Soc. *139*, 8698–8704.

37. Sun, Q., Fu, C.-W., Aguila, B., Perman, J.A., Wang, S., Huang, H.-Y., Xiao, F.-S., and Ma, S. (2018). Pore environment control and enhanced performance of enzymes infiltrated in covalent organic frameworks. J. Am. Chem. Soc. *140*, 984–992.

38. Ma, H., Liu, B., Li, B., Zhang, L., Li, Y.-G., Tan, H.-Q., Zang, H.-Y., and Zhu, G. (2016). Cationic covalent organic frameworks: a simple platform of anionic exchange for porosity tuning and proton conduction. J. Am. Chem. Soc. *138*, 5897–5903.

39. Zeng, Y., Zou, R., and Zhao, Y. (2016). Covalent organic frameworks for CO_2 capture. Adv. Mater. *28*, 2855–2873.

40. Wang, S., Wang, Q., Shao, P., Han, Y., Gao, X., Ma, L., Yuan, S., Ma, X., Zhou, J., Feng, X., and Wang, B. (2017). Exfoliation of covalent organic frameworks into few-layer redox-active nanosheets as cathode materials for lithium-ion batteries. J. Am. Chem. Soc. *139*, 4258–4261.

41. Chen, R., Shi, J.-L., Ma, Y., Lin, G., Lang, X., and Wang, C. (2019). Designed synthesis of a 2D porphyrin-based sp^2 carbon conjugated covalent organic framework for heterogeneous photocatalysis. Angew. Chem. Int. Ed. *58*, 6430–6434.

42. Lv, J., Tan, Y.-X., Xie, J., Yang, R., Yu, M., Sun, S., Li, M.-D., Yuan, D., and Wang, Y. (2018). Direct solar-to-electrochemical energy storage in a functionalized covalent organic framework. Angew. Chem. Int. Ed. *57*, 12716–12720.

43. Yang, S., Hu, W., Zhang, X., He, P., Pattengale, B., Liu, C., Cendejas, M., Hermans, I., Zhang, X., Zhang, J., and Huang, J. (2018). 2D covalent organic frameworks as intrinsic photocatalysts for visible light-driven CO_2 reduction. J. Am. Chem. Soc. *140*, 14614–14618.

44. Pachfule, P., Acharjya, A., Roeser, J., Langenhahn, T., Schwarze, M., Schomäcker, R., Thomas, A., and Schmidt, J. (2018). Diacetylene functionalized covalent organic framework (COF) for photocatalytic hydrogen generation. J. Am. Chem. Soc. *140*, 1423–1427.

45. Keller, N., Bessinger, D., Reuter, S., Calik, M., Ascherl, L., Hanusch, F.C., Auras, F., and Bein, T. (2017). Oligothiophene-bridged conjugated covalent organic frameworks. J. Am. Chem. Soc. *139*, 8194–8199.

46. Vyas, V.S., Haase, F., Stegbauer, L., Savasci, G., Podjaski, F., Ochsenfeld, C., and Lotsch, B.V. (2015). A tunable azine covalent organic framework platform for visible light-induced hydrogen generation. Nat. Commun. *6*, 8508.

47. Wei, P.-F., Qi, M.-Z., Wang, Z.-P., Ding, S.-Y., Yu, W., Liu, Q., Wang, L.-K., Wang, H.-Z., An, W.-K., and Wang, W. (2018). Benzoxazole-linked ultrastable covalent organic frameworks for photocatalysis. J. Am. Chem. Soc. *140*, 4623–4631.

48. Li, Z., Zhi, Y., Shao, P., Xia, H., Li, G., Feng, X., Chen, X., Shi, Z., and Liu, X. (2019). Covalent organic framework as an efficient, metal-free, heterogeneous photocatalyst for organic transformations under visible light. Appl. Catal. B *245*, 334–342.

49. Zhao, Y., Liu, H., Wu, C., Zhang, Z., Pan, Q., Hu, F., Wang, R., Li, P., Huang, X., and Li, Z. (2019). Fully conjugated two-dimensional sp^2-carbon covalent organic frameworks as artificial photosystem I with high efficiency. Angew. Chem. Int. Ed. *58*, 5376–5381.

50. He, J., Yin, B., Niu, H., and Cai, Y. (2018). Targeted synthesis of visible-light-driven covalent organic framework photocatalyst via molecular design and precise construction. Appl. Catal. B *239*, 147–153.

51. Wu, C., Liu, Y., Liu, H., Duan, C., Pan, Q., Zhu, J., Hu, F., Ma, X., Jiu, T., Li, Z., and Zhao, Y. (2018). Highly conjugated three-dimensional covalent organic frameworks based on spirobifluorene for perovskite solar cell enhancement. J. Am. Chem. Soc. *140*, 10016–10024.

52. Bhadra, M., Kandambeth, S., Sahoo, M.K., Addicoat, M., Balaraman, E., and Banerjee, R. (2019). Triazine functionalized porous covalent organic framework for photo-organocatalytic E-Z isomerization of olefins J. Am. Chem. Soc. *141*, 6152–6156.

53. Jin, E., Lan, Z., Jiang, Q., Geng, K., Li, G., Wang, X., and Jiang, D. (2019). 2D sp^2 carbon-conjugated covalent organic frameworks for photocatalytic hydrogen production from water. Chem *5*, 1632–1647.

54. Li, X., Gao, Q., Aneesh, J., Xu, H.-S., Chen, Z., Tang, W., Liu, C., Shi, X., Adarsh, K.V., Lu, Y., and Loh, K.P. (2018). Molecular engineering of bandgaps in covalent organic frameworks. Chem. Mater. *30*, 5743–5749.

55. Wang, X., Chen, L., Chong, S.Y., Little, M.A., Wu, Y., Zhu, W.-H., Clowes, R., Yan, Y., Zwijnenburg, M.A., Sprick, R.S., and Cooper, A.I. (2018). Sulfone-containing covalent organic frameworks for photocatalytic hydrogen evolution from water. Nat. Chem. *10*, 1180–1189.

56. Sprick, R.S., Bonillo, B., Clowes, R., Guiglion, P., Brownbill, N.J., Slater, B.J., Blanc, F., Zwijnenburg, M.A., Adams, D.J., and Cooper, A.I. (2016). Visible-light-driven hydrogen evolution using planarized conjugated polymer photocatalysts. Angew. Chem. Int. Ed. *55*, 1792–1796.

57. DeRosa, M.C., and Crutchley, R.J. (2002). Photosensitized singlet oxygen and its applications. Coord. Chem. Rev. *233-234*, 351–371.

58. Tobin, J.M., McCabe, T.J.D., Prentice, A.W., Holzer, S., Lloyd, G.O., Paterson, M.J., Arrighi, V., Cormack, P.A.G., and Vilela, F. (2017). Polymer-supported photosensitizers for oxidative organic transformations in flow and under visible light irradiation. ACS Catal. *7*, 4602–4612.

59. Thomas, S., Li, H., Zhong, C., Matsumoto, M., Dichtel, W.R., and Bredas, J.-L. (2019). Electronic structure of two-dimensional π-conjugated covalent organic frameworks. Chem. Mater. *31*, 3051–3065.

60. Wang, Z.J., Ghasimi, S., Landfester, K., and Zhang, K.A.I. (2014). Highly porous conjugated polymers for selective oxidation of organic sulfides under visible light. Chem. Commun. (Camb.) *50*, 8177–8180.

61. Battula, V.R., Singh, H., Kumar, S., Bala, I., Pal, S.K., and Kailasam, K. (2018). Natural sunlight driven oxidative homocoupling of amines by a truxene-based conjugated microporous polymer. ACS Catal. *8*, 6751–6759.

62. Wang, Z.J., Ghasimi, S., Landfester, K., and Zhang, K.A.I. (2015). Molecular structural design of conjugated microporous poly(benzooxadiazole) networks for enhanced photocatalytic activity with visible light. Adv. Mater. *27*, 6265–6270.

63. Mondloch, J.E., Katz, M.J., Isley, W.C., 3rd, Ghosh, P., Liao, P., Bury, W., Wagner, G.W., Hall, M.G., DeCoste, J.B., et al. (2015). Destruction of chemical warfare agents using metal-organic frameworks. Nat. Mater. *14*, 512–516.